

Preferential mobilisation of oxidised iron by slab-derived hydrous silicate melts

C. Tiraboschi, C. McCammon, A. Rohrbach, S. Klemme,
J. Berndt, C. Sanchez-Valle

Supplementary Information

The Supplementary Information includes:

- Materials and Methods
- Calculation of Fe^{3+} Transferred by Hydrous Melts in Subduction Zones
- Tables S-1 to S-3
- Figures S-1 to S-4
- Supplementary Information References

Materials and Methods

Starting materials and piston cylinder experiments

Natural hematite and magnetite, either as a fine-grained powder (1:1 molar ratio) or as single crystals, were employed as starting materials, together with a synthetic haplogranite glass and a source of fluid.

The haplogranite glass employed here, $\text{Na}_{0.56}\text{K}_{0.38}\text{Al}_{0.95}\text{Si}_{5.19}\text{O}_{12.2}$, is silica-rich ($\text{Si}/(\text{Si}+\text{Al}) = 0.86$) and slightly peralkaline ($(\text{Na} + \text{K})/\text{Al} = 1.13$; $\text{Na}/\text{K} = 0.9$) as shown in Table S-1 (Ardia *et al.*, 2008, 2014).

Experiments were conducted in an end-loaded piston cylinder apparatus at WWU Münster with two different fluid systems: i) H_2O -only or ii) H_2O -NaCl solution with a concentration of 1.5 m NaCl (~8 wt. % NaCl, ~4.9 wt. % Cl) to approximate the salinity of island-arc setting slab-derived fluids (*e.g.*, Kent *et al.*, 2002). Variable amounts of fluid were added to the experimental charges (Table S-1) to guarantee hydrous conditions of the coexisting melt at run conditions, *i.e.* below the critical curve for the haplogranite- H_2O system (Bureau and Keppler, 1999; Fig. 1). Run duration varied from 24 hours for high-temperature experiments (*i.e.* 900 °C) to 72 hours in low-temperature runs (*i.e.* 700 °C) to ensure equilibration (see discussion below).



The oxygen fugacity conditions were constrained by the simultaneous presence of magnetite and hematite (HM buffer), which is between -11.3 (2 GPa, 700 °C, ΔFMQ 3.8) and -6.4 (1 GPa, 950 °C, ΔFMQ 4.8) expressed as $\log f\text{O}_2$ (Table 1). Fixing the oxygen fugacity conditions brings some important constraints to our experimental strategy, as at buffered conditions the only iron exchange in the experimental capsule would derive from the dissolution process, and not from redox reactions occurring between hematite and magnetite. Moreover, the imposed redox conditions are comprised into the range of oxygen fugacities expected in subduction mélanges (see Cannà and Malaspina, 2018 and ref. therein).

Oxygen fugacities at the experimental conditions are expressed as $\log f\text{O}_2$ and were calculated employing the software package *Perple_X* (Connolly, 1995) and the thermodynamic dataset of Holland and Powell (1998). In the experimental runs in which only magnetite or hematite are present the oxygen fugacity is unconstrained.

Starting materials (*i.e.* hematite, magnetite, glass, and fluid) were loaded in gold capsules (3 mm outer diameter, ~ 7 mm length), mounted on steel support stored at -20 °C, and welded shut, to avoid fluid loss during welding. Capsules were loaded in a MgO–Pyrex–talc assembly. The temperature was measured through W_{97}Re_3 – $\text{W}_{75}\text{Re}_{25}$ thermocouples and is considered accurate within ± 10 °C. Pressure calibration of the apparatus is based on the quartz-coesite transition (Bose and Ganguly, 1995) and the $\text{MgCr}_2\text{O}_4 + \text{SiO}_2 = \text{MgSiO}_3 + \text{Cr}_2\text{O}_3$ reaction (Klemme and O'Neill, 1997), and a friction correction of -13% was applied to the nominal pressure. Pressures are considered accurate to 0.01 GPa. In all runs, fragments of the original hematite and/or magnetite were recovered from the capsule after quench, demonstrating saturation during the experiment. Experiments performed at buffered conditions showed no formation of new crystals of magnetite or hematite. All runs showed excess fluid upon capsule puncturing and the presence of water in the recovered glass fragment was confirmed by Raman spectroscopy.

Attainment of equilibrium in the experimental runs

Attainment of equilibrium conditions was confirmed by time series experiments performed at the same pressure, temperature, and oxygen fugacity conditions, with run durations ranging from 24 to 72 hours. For instance, experiments performed within 24 hours (GHM1) and 72 hours (GHM5) at 1 GPa and 800 °C display similar values of FeO in the quenched glass within error (Table S-1), showing no major difference even for shorter experimental runs. Moreover, experiments performed at similar P , T , and $f\text{O}_2$ conditions employing either powders or single-crystals of hematite and magnetite yield comparable FeO values (*e.g.*, GHM5 and GHM2, Table S-1), demonstrating little effect of the grain size on FeO content as well as equilibration during the experiments.

Achievement of redox equilibrium in our experiments is expected due to the long run duration, *i.e.* above 24 hours, which is significantly longer than the redox equilibration times of 3–10 hours reported for hydrous metaluminous or peralkaline melts with approximately 1–3 wt. % of total FeO at 800 °C and 0.2 GPa by Gaillard *et al.* (2002). Moreover, the redox ratio of iron and the hyperfine parameters of ferric and ferrous iron determined by Mössbauer spectroscopy in the recovered glasses should not be affected by fast quenching rates (Mysen, 2006).

Analytical techniques

Major element concentrations of quenched glasses, hematite, and magnetite were determined with a 5-spectrometer JEOL JXA 8530F electron microprobe (EMP) at the Institute of Mineralogy, WWU Münster. Analyses of the quenched glasses were performed with an accelerating voltage of 15 keV and a beam current of 10 nA, with variable beam sizes ranging from 5 to 20 μm on homogenous parts of the glass, *i.e.* free from Fe oxides grains and vapour bubbles (Fig. S-1a,b). The homogeneity of the glasses was checked by repeated analyses in different areas of the sample and by optical examination to confirm the absence of microscopic mineral phases. The signal from Na was monitored during the measurements and no significant loss was observed. Samples major elements analyses are summarised in Table S-1.

Mössbauer absorption spectra were collected at Bayerisches Geoinstitut (BGI), University of Bayreuth on samples GHM9, GHM10, GH2, and GM1, which present high FeO content. Glass pieces were mounted on plastic film using clear nail varnish to form a mosaic of approximately 2 mm diameter and 1 mm thick. This corresponds to a Mössbauer thickness of roughly 4 mg Fe/cm², which is close to the optimum for these compositions. Spectra were collected in



transmission mode on a constant acceleration Mössbauer spectrometer with a nominal 370 MBq ^{57}Co point source in a 12 μm Rh matrix with active dimension of $500 \times 500 \mu\text{m}^2$. The velocity scale was calibrated with Fe foil. Spectra were collected at room temperature over a velocity scale of $\pm 5 \text{ mm/s}$ with measuring times of approximately 7 days each. Spectra were fitted using MossA software (Prescher *et al.*, 2012).

Thermodynamic modelling

We employed the DEW model (Sverjensky *et al.*, 2014; Huang and Sverjensky, 2019; Sverjensky, 2019) coupled with the Fortran code EQ3NR (Wolery, 1992) to calculate the solubility of hematite and magnetite in H_2O , H_2O -NaCl fluids and fluids equilibrated with a dissolved silica species. The DEW model employs the Helgeson-Kirkham-Flowers (HKF) equations of state for aqueous species (Helgeson *et al.*, 1981; Shock and Helgeson, 1988, 1990; Tanger and Helgeson, 1988; Shock *et al.*, 1989, 1997) together with revised predictive correlations between the equation of state coefficients and the standard partial molal properties of aqueous species (Facq *et al.*, 2014; Sverjensky *et al.*, 2014; Sverjensky, 2019) to calculate the apparent standard partial molal Gibbs free energies of aqueous species at high pressures and temperatures. Equilibrium constants are then incorporated in the Fortran code EQ3NR (Wolery, 1992) to compute aqueous speciation and solubility models, providing total dissolved concentrations of each element and the saturation state of the associated fluid with respect to the minerals in the system.

The first set of solubilities was calculated from 700 to 1000 °C and from 1 to 2 GPa considering the H_2O -only and the H_2O -NaCl systems. The input file was constructed in order to have hematite and magnetite coexisting at fixed oxygen fugacity conditions. The second set of calculations was performed by adding appropriate amounts of $\text{Si}(\text{OH})_4$, to account for the presence of a silicate melt and to evaluate the possible influence of dissolved silica on iron transport. Results from modelling are reported in Table S-3.

Since to our knowledge, no experimental data are available for the solubility of haplogranite melts in H_2O and H_2O -NaCl fluids, the composition of the aqueous fluid was estimated from experimental data (see Louvel *et al.*, 2020) on albite dissolution in H_2O (Manning *et al.*, 2010; Wohlers *et al.*, 2011). Silica contents in the fluid were exponentially extrapolated to higher temperatures (*i.e.* 900 °C) following Manning *et al.* (2010), which showed a strong increase in the solute content at near-solidus conditions in the system albite + paragonite + quartz + H_2O , possibly due to the presence of more polymerized species (Newton and Manning, 2008).

Mössbauer absorption results

The Mössbauer spectra recorded on the four investigated samples are shown in Figure S-2 and the results are presented below. The Mössbauer spectra fitting parameters, including the centre shift (CS) and quadrupole splitting (QS) (Fig. S-3), as well as the calculated $\text{Fe}^{3+}/\text{Fe}_{\text{tot}}$ ratios are summarised in Table S-2.

GHM9

The spectrum (Fig. S-2a) can be fit to two doublets with Voigt lineshape (Gaussian distribution of Lorentzians). The green doublet is assigned to Fe^{3+} and the blue doublet to Fe^{2+} . The blue doublet has a centre shift of 1.16, which is higher than expected for a glass. This can be attributed to its presence as precipitates from the fluid phase. The bulk value of $\text{Fe}^{3+}/\text{Fe}_{\text{tot}}$ can be calculated from the relative areas as 0.79 ± 0.04 .

GHM10

The spectrum can be fit to two doublets as sample GHM9, with the addition of a sextet (Fig. S-2b). Only the inner four lines of the sextet are observed due to small velocity scale, but all positions are consistent with hematite. The two doublets have the same hyperfine parameters (centre shift and quadrupole splitting) as those in sample GHM9 (Table S-2), indicating that Fe^{2+} is mainly present as precipitates from the fluid phase. The bulk value of $\text{Fe}^{3+}/\text{Fe}_{\text{tot}}$ considering the doublets only and excluding the hematite from the calculation is 0.45 ± 0.07 .



GH2

The prominent doublet (dark green) has parameters consistent with tetrahedral Fe³⁺ (Fig. S-2c). A broad doublet (blue) is consistent with Fe³⁺ but with higher coordination. A broad doublet with higher centre shift and quadrupole splitting (medium green) is assigned to Fe²⁺, also in this case attributed to the presence of precipitates. Magnetic peaks could be fit to the data and parameters correspond to hematite. The calculated Fe³⁺/Fe_{tot} is retrieved from relative areas excluding the contribution of hematite and corresponds to 0.73±0.22.

GMI

Doublets assigned to glass components are similar to those in the previous spectrum except that the Fe²⁺ doublet is noticeably more intense compared to GH2 (Fig. S-2d). There is a broad absorption (blue) that could arise from a weak magnetic interaction, for example very small particles of ferric iron oxide (around a few tens of nanometres grain size). The Fe³⁺/Fe_{tot} is calculated from relative areas, excluding the contribution of the small particles of iron oxides, and corresponds to 0.64±0.15.

Overall, the data show that Fe³⁺ is mainly present in the melt structure, probably in more than one coordination environment. Parameters reported in Table S-2 are consistent with Fe³⁺ in tetrahedral coordination and possibly higher values (IV or VI, or a mixture of both). On the other hand, Fe²⁺ seems to be present for the most part as precipitates from the aqueous fluid, as shown by high values of centre shift (CS) and quadrupole splitting (QS) (Fig. S-3). However, due to the Fe²⁺ broad absorption, it is not possible to exclude the presence of Fe²⁺ also in the melt structure.

Unbuffered experimental runs

The two unbuffered experiments (Fig. S-1c,d) resulted in slightly lower Fe³⁺/FeO_{tot} ratios: 0.73±0.22 for the quenched glass in equilibrium with hematite and 0.64±0.15 for the glass in equilibrium with magnetite at 1 GPa and 900 °C in the H₂O + melt system. The difference is mainly ascribable to the Fe²⁺ content, as the calculated amount of Fe³⁺ in the glass is similar for both experiments (*i.e.* 1.10 wt. % for magnetite + hydrous melt, and 1.15 wt. % for hematite + hydrous melt experiment, see Table S-1). However, due to the low amount of total iron in the system, which leads to a significant error in the retrieved Fe³⁺/Fe_{tot} ratio obtained by Mössbauer spectroscopy, it is difficult to assess if the two unbuffered experiments equilibrated at the same Fe³⁺/Fe²⁺ ratio.

These results highlight the importance to investigate the dissolution process at buffered conditions, to avoid redox reactions between hematite and magnetite, which could influence the amount of iron mobilised in the system. For instance, in the hematite-only experiment, Mössbauer absorption spectra indicate the presence of Fe²⁺, which likely derives from a redox reaction. Moreover, some redox reactions probably also occur in the magnetite-only experiment, which showed some reaction rims suggesting the formation of hematite (Fig. S-1d).

Calculation of Fe³⁺ Transferred by Hydrous Melts in Subduction Zones

The experimental results presented were further employed to provide constraints on the amount of Fe³⁺ transferred by hydrous melts from hematite and magnetite, which is crucial information to evaluate the redox budget of subduction zones (Evans, 2006, 2012; Evans and Tomkins, 2011).

Here we considered the Fe³⁺ content at 2 GPa and 900 °C (sample GHM9 and GHM10) in both systems: H₂O + melt and H₂O-NaCl + melt to constrain the Fe³⁺ fluxes associated with hematite–magnetite dissolution in hydrous melts at subduction zone conditions.

The Fe₂O₃ content in the quenched glass was calculated from the Fe³⁺/Fe_{tot} ratio derived from the Mössbauer absorption spectra and from the total FeO content obtained by electron microprobe analyses (Table 1 and Table S-1). In the H₂O + melt system, the Fe₂O₃ corresponds to 1.59 wt. % while in the H₂O-NaCl + melt system equals 0.98 wt. % (Fig. S-4).



Because the iron redox ratios in silicate melts are linearly proportional to the oxygen fugacity conditions on a logarithmic scale (Kress and Carmichael, 1991; Wilke *et al.*, 2002; Botcharnikov *et al.*, 2005) we can extrapolate the possible Fe³⁺ content in hydrous melt in equilibrium with magnetite and hematite to lower temperature conditions, in order to approximate conditions compatible with hot subduction geotherms paths (*e.g.*, Syracuse *et al.* 2010) as shown in Fig. 1.

We considered two possible correlations between the Fe³⁺/Fe²⁺ ratio and the oxygen fugacity. The first one is derived from the empirical equation of Kress and Carmichael (1991) and it has been calculated from experimental data at 2 GPa and 900 °C. The second curve slope considered is derived from experimental Mössbauer absorption data of hydrous silicate melts from Wilke *et al.* (2002), obtained at 0.5 GPa and temperatures of 850 and 950 °C. The two different linear correlations define two areas, which represent the possible Fe³⁺/Fe²⁺ ratios depending on the oxygen fugacity conditions. Since the simultaneous presence of hematite and magnetite in the system define the *f*O₂ at fixed pressure and temperature, it is possible to calculate the possible Fe₂O₃ content of hydrous melts in equilibrium with hematite and magnetite to lower temperature conditions, more compatible with a hot subducting slab geotherm (see Fig. 1).

In the H₂O + melt system the expected Fe³⁺ content calculated ranges from 0.15 to 0.23 wt. %, up to the measured values of 1.59 wt. % at 2 GPa and 900 °C (*f*O₂ = -6.9, ΔFMQ 4.0). In the H₂O-NaCl + melt system the retrieved Fe³⁺ ranges from 0.05 to 0.08 wt. % at 2 GPa and 700 °C (*f*O₂ = -11.5, ΔFMQ 3.8), reaching values of 0.98 wt. % at 2 GPa and 900 °C (*f*O₂ = -6.9, ΔFMQ 4.0). These values provide the amount of oxidised iron mobilised from hematite and magnetite dissolution by hydrous silicate melts at conditions compatible with a hot subduction slab.

Comparison with previous studies

The FeO concentrations in hydrous haplogranite glasses retrieved here compare well with the results from experimental studies of sediment melting at sub-arc conditions (Hermann *et al.*, 2006; Hermann and Spandler, 2008). These experiments, conducted at slightly higher pressures, *i.e.* 2.5 GPa, report FeO contents in the quenched hydrous glass ranging from 1.04 wt. % (16 wt. % H₂O) at 750 °C to 1.26 wt. % at 800 °C (10 wt. % H₂O). For comparison, we report a FeO content of 0.96 wt. % at 2 GPa, 800 °C in the H₂O-only system (9.39 wt. % H₂O).

Moreover, our results are also consistent with FeO contents determined in natural melt inclusions from mantle xenoliths. Although mantle xenoliths from the subarc upper mantle are quite rare, few examples can be considered for comparison. For instance, hornblende peridotite xenoliths from central Mexico (Blatter and Carmichael, 1998) show oxygen fugacity comprises between ΔFMQ 1.5 and 2.4, locally up to 4 in presence of hematite and magnetite. The FeO content in the silicate glass, *i.e.* 1.02 wt. %, is compatible with our results at similar pressure and temperature conditions (*i.e.* 1.5 GPa and 800 °C). Similar FeO content, 1.27 wt. %, and 8.1 wt. % H₂O, has been also measured in melt inclusions from mantle xenoliths from the Avacha volcano in Kamchatka (Ionov *et al.*, 2011).

Geological environments

The investigated experimental system represents a simplified subduction slab setting, in which Fe-oxides interact with a haplogranitic composition. The Fe-source is exclusively represented by magnetite and hematite, which are common in subduction zone settings, for instance in serpentinites (*e.g.*, Carbonin *et al.*, 2015; Debret *et al.*, 2015) and in metasediments (*e.g.*, Tumiati *et al.*, 2015; Ague *et al.*, 2022). Our results thus have direct implications for two possible geological environments where interactions between hydrous (haplo)granitic melts with magnetite–hematite occurs. First, the melt is produced by magnetite and hematite-bearing metasediments. Metasediments constitute a layer thick up to 400 m (Van Keken *et al.*, 2011) above the altered oceanic crust, and often contain oxidised Fe³⁺-bearing sedimentary detritus (Ague *et al.*, 2022 and ref. therein). Highly oxidised metasediments from exhumed subduction complexes have been observed in the Alps (Tumiati *et al.*, 2015) and in other locations (see Cannà and Malaspina, 2018). Recently Ague *et al.* (2022) showed that highly oxidised metasedimentary rocks, containing hematite and magnetite, have the capacity of oxidising the fluid released from the slab. The granitic melt generated at these conditions would be in equilibrium with magnetite and hematite, consequently, it will efficiently dissolve Fe from these phases, and would transfer the oxidised signature directly to the mantle wedge. Second, the hydrous silicate melt is generated by metasediment slices present in the subduction mélange (Marschall and Schumacher, 2012; Nielsen and Marschall, 2017),



and interacts with serpentinite slices. Similarly to the first environment, the resulting melt will then reach the mantle wedge and efficiently transfer Fe^{3+} to the source of arc magmas.



Supplementary Tables

Table S-1 Major element compositions (in wt. %) of the starting haplogranitic composition (HGG) and quenched glasses determined by electron microprobe. Uncertainties are reported below the average values for each glass as 1 standard deviation of n ($10 < n < 50$) analyses performed on the glass. H₂O concentrations were not analysed; the reported values are obtained by subtracting the total of major element analyses from 100. FeO* and Fe₂O₃* refer to the calculated amounts of Fe²⁺ and Fe³⁺ considering the Fe³⁺/Fe_{tot} ratios obtained by Mössbauer spectroscopy.

| | <i>P</i> (GPa) | <i>T</i> (°C) | run time (h) | starting fluid | fluid (wt. %) | Na ₂ O | MgO | Al ₂ O ₃ | SiO ₂ | K ₂ O | CaO | Cl | FeO | TiO ₂ | Cr ₂ O ₃ | MnO | Total | H ₂ O | FeO* | Fe ₂ O ₃ * |
|-------|----------------|---------------|--------------|-----------------------------|---------------|-------------------|------|--------------------------------|------------------|------------------|------|------|------|------------------|--------------------------------|------|-------|------------------|------|----------------------------------|
| HGG | | | | | | 4.52 | 0.00 | 11.73 | 78.53 | 4.47 | 0.01 | 0.01 | 0.02 | 0.03 | 0.01 | 0.01 | 99.37 | | | |
| | | | | | | 0.10 | 0.01 | 0.06 | 0.16 | 0.11 | 0.01 | 0.01 | 0.01 | 0.03 | 0.01 | 0.01 | 0.21 | | | |
| GHM3 | 1 | 700 | 48 | H ₂ O | 19.37 | 3.34 | 0.01 | 10.72 | 71.29 | 3.85 | 0.03 | 0.00 | 0.60 | 0.02 | 0.01 | 0.01 | 89.88 | 10.12 | | |
| | | | | | | 0.17 | 0.01 | 0.14 | 0.69 | 0.09 | 0.02 | 0.00 | 0.21 | 0.03 | 0.01 | 0.02 | 0.85 | | | |
| GHM6 | 1 | 700 | 48 | 1.5 m H ₂ O-NaCl | 27.39 | 3.73 | 0.00 | 11.46 | 68.76 | 4.28 | 0.02 | 0.05 | 0.75 | 0.02 | 0.02 | 0.01 | 89.11 | 10.89 | | |
| | | | | | | 0.32 | 0.01 | 0.15 | 0.64 | 0.27 | 0.02 | 0.01 | 0.08 | 0.03 | 0.02 | 0.02 | 0.34 | | | |
| GHM1 | 1 | 800 | 24 | H ₂ O | 41.94 | 2.94 | 0.01 | 10.82 | 71.34 | 3.92 | 0.04 | 0.01 | 1.04 | 0.02 | 0.01 | 0.03 | 90.17 | 9.83 | | |
| | | | | | | 0.32 | 0.01 | 0.15 | 0.96 | 0.11 | 0.02 | 0.01 | 0.12 | 0.02 | 0.02 | 0.03 | 0.70 | | | |
| GHM7 | 1 | 800 | 24 | 1.5 m H ₂ O-NaCl | 21.43 | 2.59 | 0.02 | 10.74 | 72.17 | 4.52 | 0.04 | 0.11 | 1.50 | 0.01 | 0.01 | 0.04 | 91.70 | 8.30 | | |
| | | | | | | 0.48 | 0.02 | 0.14 | 1.02 | 0.56 | 0.02 | 0.02 | 0.31 | 0.01 | 0.02 | 0.02 | 1.41 | | | |
| GHM5 | 1 | 800 | 72 | H ₂ O | 18.10 | 3.37 | 0.05 | 10.54 | 71.59 | 3.95 | 0.02 | 0.00 | 1.22 | 0.03 | 0.01 | 0.03 | 90.82 | 9.18 | | |
| | | | | | | 0.13 | 0.02 | 0.16 | 0.49 | 0.09 | 0.01 | 0.00 | 0.24 | 0.02 | 0.01 | 0.02 | 0.67 | | | |
| GHM2* | 1 | 800 | 72 | H ₂ O | 17.83 | 0.82 | 0.04 | 11.18 | 72.96 | 3.47 | 0.11 | 0.01 | 1.23 | 0.01 | 0.01 | 0.03 | 89.87 | 10.13 | | |
| | | | | | | 0.33 | 0.01 | 0.22 | 0.88 | 0.78 | 0.03 | 0.01 | 0.06 | 0.02 | 0.01 | 0.02 | 1.25 | | | |
| GHM4 | 1 | 900 | 24 | H ₂ O | 23.86 | 3.13 | 0.02 | 10.53 | 70.38 | 3.89 | 0.04 | 0.00 | 1.82 | 0.03 | 0.01 | 0.04 | 89.90 | 10.10 | | |
| | | | | | | 0.21 | 0.02 | 0.10 | 0.49 | 0.09 | 0.02 | 0.00 | 0.11 | 0.03 | 0.01 | 0.02 | 0.66 | | | |
| GHM11 | 1 | 900 | 24 | 1.5 m H ₂ O-NaCl | 27.65 | 2.70 | 0.01 | 10.70 | 72.70 | 3.70 | 0.03 | 0.15 | 2.17 | 0.02 | 0.01 | 0.04 | 92.23 | 7.77 | | |
| | | | | | | 0.30 | 0.01 | 0.14 | 0.81 | 0.31 | 0.02 | 0.08 | 0.26 | 0.03 | 0.01 | 0.02 | 1.11 | | | |
| GM1* | 1 | 900 | 24 | H ₂ O | 31.97 | 2.89 | 0.03 | 10.21 | 71.04 | 3.79 | 0.02 | 0.00 | 1.61 | 0.01 | 0.01 | 0.03 | 89.68 | 10.32 | 0.62 | 1.10 |
| | | | | | | 0.26 | 0.01 | 0.13 | 0.56 | 0.13 | 0.01 | 0.01 | 0.09 | 0.02 | 0.01 | 0.02 | 0.57 | | | |
| GH2* | 1 | 900 | 24 | H ₂ O | 47.06 | 2.50 | 0.02 | 10.81 | 72.96 | 3.66 | 0.01 | 0.01 | 1.42 | 0.02 | 0.01 | 0.01 | 91.44 | 8.56 | 0.38 | 1.15 |



| | | | | | | | | | | | | | | | | | | | | |
|--------|---|-----|----|-----------------------------|-------|------|------|-------|-------|------|------|------|------|------|------|------|-------|-------|------|------|
| GHM13* | 1 | 950 | 24 | H ₂ O | 18.69 | 0.39 | 0.01 | 0.11 | 0.70 | 0.24 | 0.01 | 0.01 | 0.13 | 0.02 | 0.01 | 0.01 | 0.70 | | | |
| | | | | | | 2.99 | 0.01 | 10.10 | 70.95 | 3.76 | 0.05 | 0.01 | 1.96 | 0.02 | 0.01 | 0.09 | 89.99 | 10.01 | | |
| | | | | | | 0.24 | 0.01 | 0.17 | 0.96 | 0.12 | 0.02 | 0.01 | 0.04 | 0.02 | 0.01 | 0.02 | 1.12 | | | |
| GHM15* | 1 | 950 | 24 | 1.5 m H ₂ O-NaCl | 30.77 | 2.83 | 0.01 | 9.99 | 70.77 | 3.53 | 0.03 | 0.17 | 2.40 | 0.02 | 0.01 | 0.05 | 89.87 | 10.13 | | |
| | | | | | | 0.87 | 0.01 | 0.22 | 1.03 | 0.54 | 0.02 | 0.07 | 0.12 | 0.02 | 0.01 | 0.02 | 0.67 | | | |
| GHM19 | 2 | 700 | 48 | 1.5 m H ₂ O-NaCl | 27.81 | 3.96 | 0.01 | 13.53 | 70.15 | 3.92 | 0.00 | 0.21 | 0.60 | 0.02 | 0.02 | 0.02 | 92.46 | 7.54 | | |
| | | | | | | 0.34 | 0.01 | 0.18 | 0.45 | 0.19 | 0.01 | 0.05 | 0.09 | 0.03 | 0.02 | 0.01 | 0.53 | | | |
| GHM20* | 2 | 800 | 24 | H ₂ O | 21.76 | 2.02 | 0.02 | 10.64 | 74.03 | 2.64 | 0.02 | 0.02 | 0.96 | 0.02 | 0.01 | 0.05 | 90.61 | 9.39 | | |
| | | | | | | 0.31 | 0.01 | 0.20 | 1.69 | 0.32 | 0.02 | 0.02 | 0.11 | 0.03 | 0.01 | 0.02 | 1.74 | | | |
| GHM9* | 2 | 900 | 24 | H ₂ O | 23.56 | 2.87 | 0.02 | 10.61 | 73.32 | 3.90 | 0.02 | 0.01 | 1.85 | 0.02 | 0.01 | 0.04 | 92.66 | 7.34 | 0.42 | 1.59 |
| | | | | | | 0.52 | 0.01 | 0.27 | 0.99 | 0.19 | 0.01 | 0.01 | 0.18 | 0.03 | 0.01 | 0.02 | 1.00 | | | |
| GHM10* | 2 | 900 | 24 | 1.5 m H ₂ O-NaCl | 29.29 | 2.25 | 0.09 | 10.56 | 72.12 | 3.78 | 0.04 | 0.18 | 2.07 | 0.01 | 0.01 | 0.04 | 91.14 | 8.86 | 1.19 | 0.98 |
| | | | | | | 0.43 | 0.05 | 0.49 | 2.41 | 0.20 | 0.02 | 0.09 | 0.41 | 0.02 | 0.02 | 0.01 | 2.66 | | | |



Table S-2 Hyperfine parameter values derived from fits of Mössbauer absorption spectra. CS: centre shift; FWHM: full width at half maximum; Int: relative area; QS: quadrupole splitting; BHF: hyperfine magnetic splitting.

| | | CS (mm/s) | Error (mm/s) | FWHM (mm/s) | Error (mm/s) | Int | Error | QS (mm/s) | Error (mm/s) | BHF (T) | Error (T) | Fe ³⁺ /Fe _{tot} |
|-------|---------------------------------|--------------|-----------------|----------------|-----------------|------|-------|--------------|-----------------|------------|--------------|-------------------------------------|
| GHM9 | Fe ³⁺ | 0.33 | 0.02 | 0.64 | 0.09 | 0.79 | 0.04 | 0.94 | 0.04 | - | - | 0.79±0.04 |
| | Fe ²⁺ | 1.16 | 0.03 | 0.34 | 0.08 | 0.21 | 0.04 | 2.46 | 0.06 | - | - | |
| GHM10 | Fe ³⁺ | 0.31 | 0.11 | 0.65 | - | 0.31 | 0.07 | 0.84 | 0.23 | - | - | 0.45±0.07 |
| | Fe ³⁺ in hematite | 0.33 | 0.04 | 0.21 | 0.19 | 0.31 | 0.11 | -0.21 | - | 50.58 | 0.48 | |
| | Fe ²⁺ | 1.14 | 0.05 | 0.37 | 0.19 | 0.38 | 0.08 | 2.50 | 0.11 | - | - | |
| GH2 | ^{IV} Fe ³⁺ | 0.33 | 0.04 | 0.19 | 0.12 | 0.10 | 0.10 | -0.21 | - | 50.4 | 0.5 | 0.73±0.22 |
| | ^{VI} Fe ³⁺ | 0.13 | 0.02 | 0.30 | 0.11 | 0.24 | 0.25 | 0.57 | 0.04 | - | - | |
| | Fe ³⁺ in hematite | 0.33 | 0.17 | 0.92 | 0.46 | 0.42 | 0.27 | 0.86 | 0.33 | - | - | |
| | Fe ²⁺ | 1.14 | 0.29 | 0.92 | 0.47 | 0.24 | 0.22 | 2.48 | 0.59 | - | - | |
| GM1 | Fe ³⁺ | 0.3 | 0.4 | 3.3 | 8.8 | 0.59 | 0.31 | 0 | - | 4 | 57 | 0.64±0.15 |
| | ^{IV} Fe ³⁺ | 0.11 | 0.02 | 0.35 | 0.07 | 0.18 | 0.18 | 0.56 | 0.05 | - | - | |
| | ^{VI} Fe ³⁺ | 0.38 | 0.16 | 0.49 | 0.37 | 0.08 | 0.24 | 0.72 | 0.20 | - | - | |
| | Fe ²⁺ | 1.07 | 0.16 | 0.79 | 0.18 | 0.14 | 0.15 | 2.45 | 0.40 | - | - | |



Table S-3 Solubility of hematite and magnetite in H₂O and H₂O-NaCl fluids at 1–2 GPa and from 700 to 1000 °C calculated with the DEW model. Solubility values are given as mol/kg of Fe. Si(OH)₄ contents are also given as mol/kg.

| Hematite and magnetite solubility in H ₂ O and H ₂ O-NaCl | | | | | | | |
|--|------------------|----------|----------|-----------------------|-------|-------|---------------------------|
| T (°C) | H ₂ O | 1 GPa | 2 GPa | H ₂ O-NaCl | 1 GPa | 2 GPa | |
| 700 | | 5.48E-07 | 1.10E-05 | | 0.004 | 0.010 | |
| 800 | | 2.97E-07 | 5.30E-06 | | 0.008 | 0.018 | |
| 900 | | 1.77E-07 | 2.81E-06 | | 0.016 | 0.032 | |
| 1000 | | 1.21E-07 | 1.70E-06 | | 0.028 | 0.053 | |
| Hematite and magnetite solubility in H ₂ O and H ₂ O-NaCl + dissolved silica | | | | | | | |
| T (°C) | H ₂ O | 1 GPa | 2 GPa | H ₂ O-NaCl | 1 GPa | 2 GPa | Si(OH) ₄ added |
| 700 | | 0.013 | 0.043 | | 0.035 | 0.076 | 1.5 |
| 800 | | 0.014 | 0.050 | | 0.044 | 0.095 | 2.4 |
| 900 | | 0.014 | 0.057 | | 0.054 | 0.118 | 5.0 |
| 1000 | | 0.014 | 0.064 | | 0.067 | 0.149 | 13.0 |



Supplementary Figures

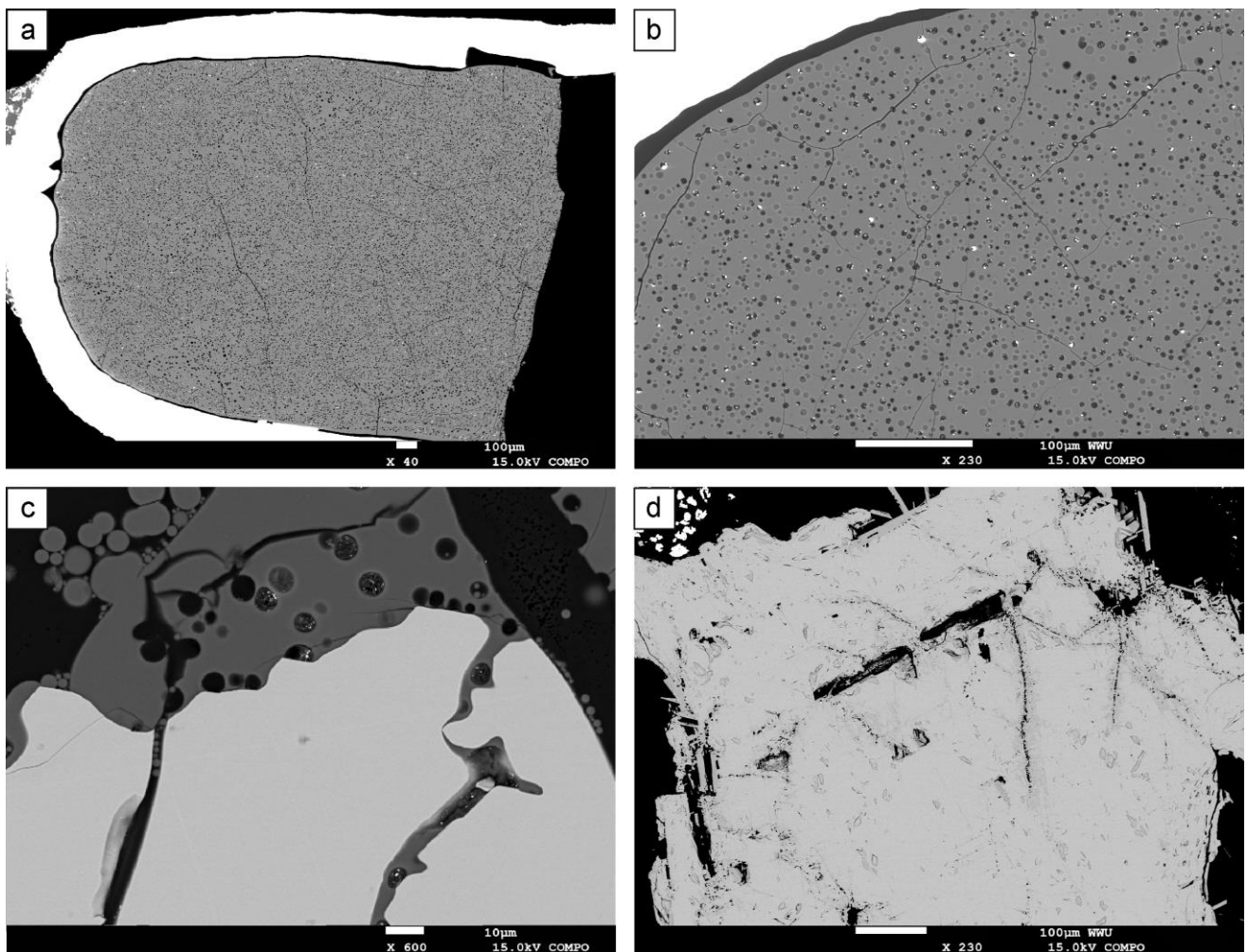


Figure S-1 Backscattered electron images of representative run products: **(a)** quenched hydrous silicate melt ($P = 1$ GPa; $T = 950$ °C, sample GHM13); **(b)** magnified detail of quenched hydrous silicate melt shown in Fig. S-1a. The bright spots are Fe-bearing precipitates, localised in vapor bubbles; **(c)** dissolution feature on a hematite crystal ($P = 1$ GPa, $T = 900$ °C, sample GH2); **(d)** dissolution features on a magnetite crystal ($P = 1$ GPa, $T = 900$ °C, sample GM1).

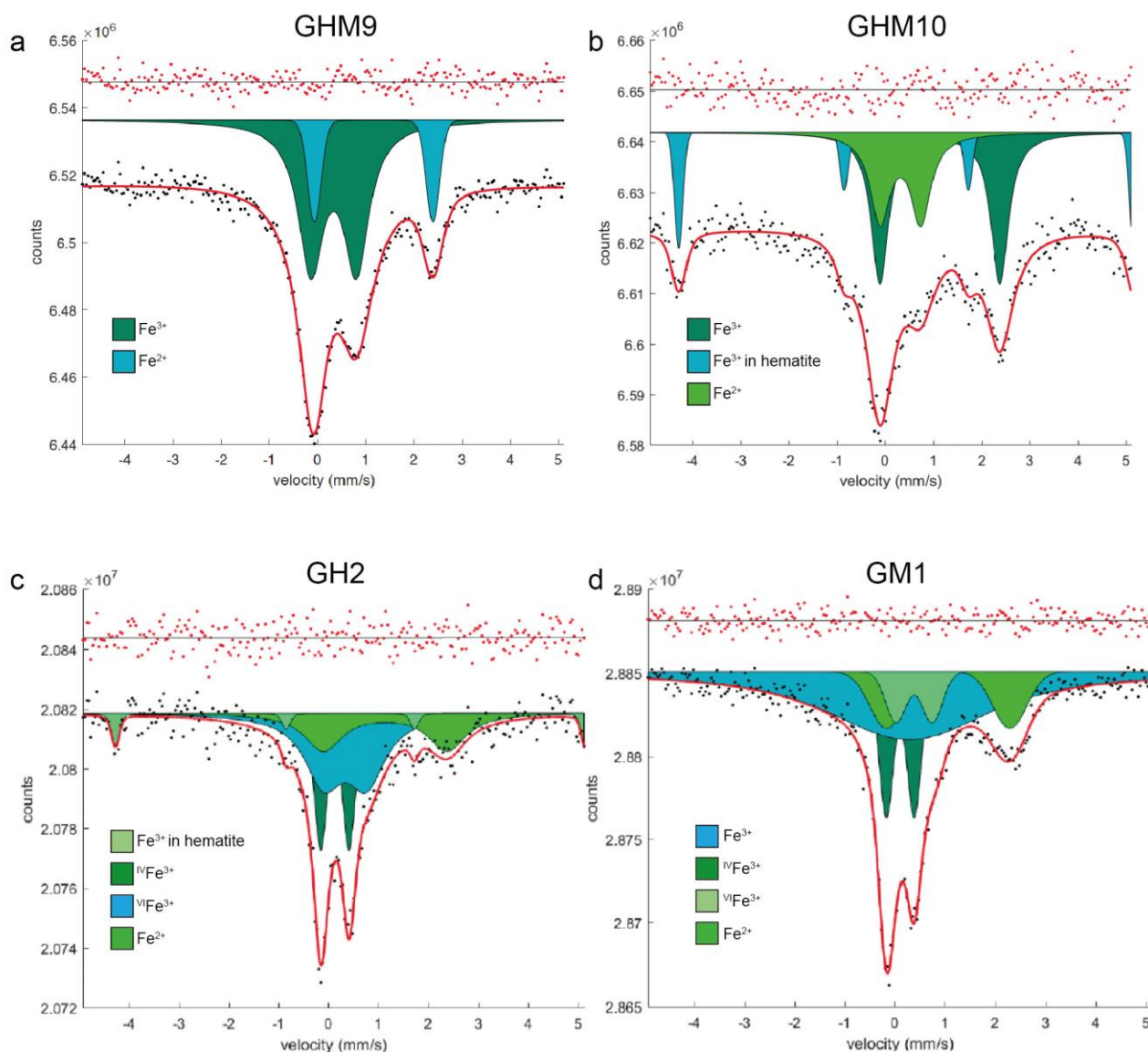


Figure S-2 Mössbauer absorption spectra (a) sample GHM9 ($P = 2$ GPa, $T = 900$ °C) (b) sample GHM10 ($P = 2$ GPa, $T = 900$ °C) (b) sample GH2 ($P = 1$ GPa, $T = 900$ °C) (b) sample GM1 ($P = 1$ GPa, $T = 900$ °C).



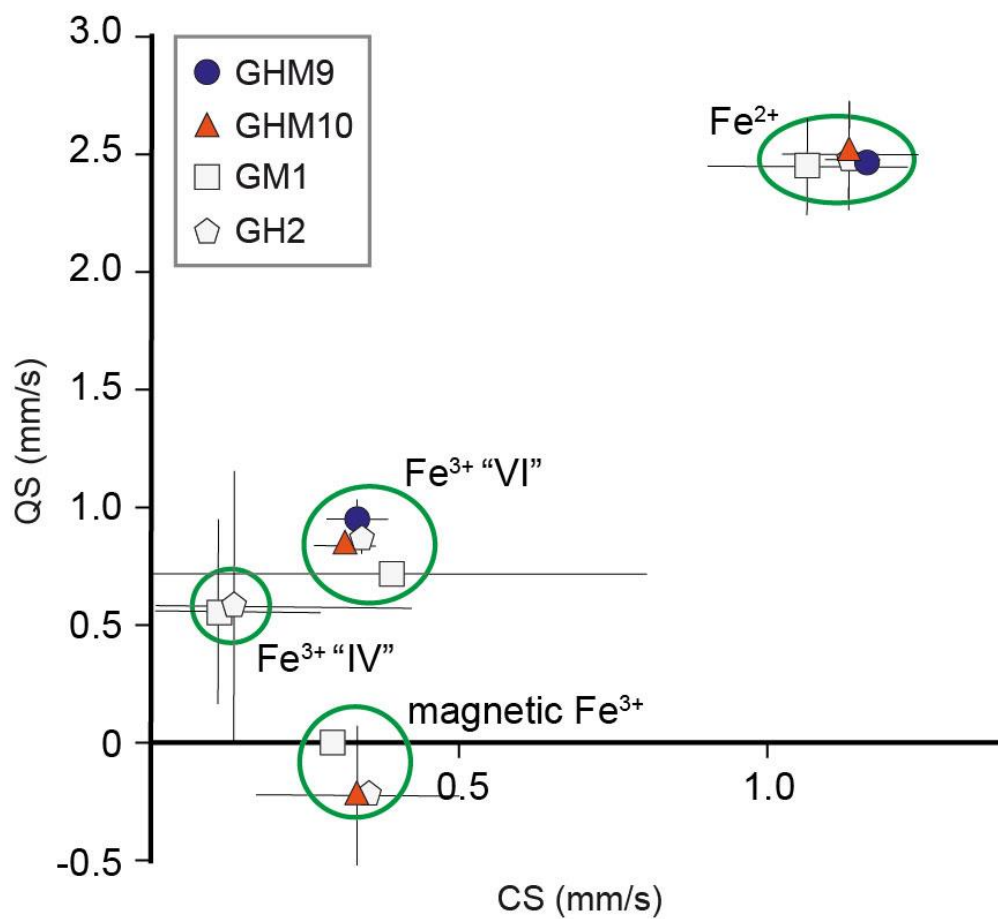


Figure S-3 Centre shift versus quadrupole splitting values derived from fits of the Mössbauer data.

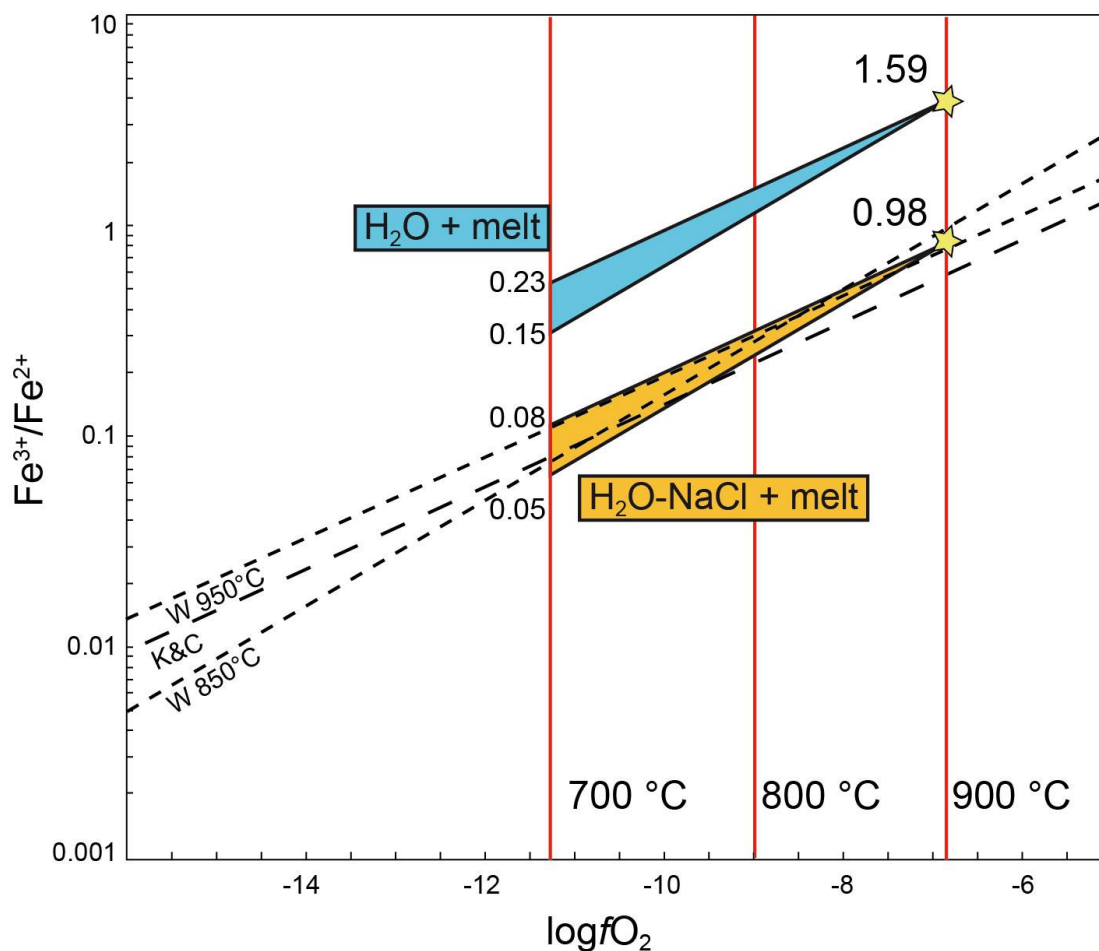


Figure S-4 Oxygen fugacity (reported as $\log f_{\text{O}_2}$) plotted versus $\text{Fe}^{3+}/\text{Fe}^{2+}$ ratios. $\text{Fe}^{3+}/\text{Fe}^{2+}$ ratios determined from Mössbauer spectra at 2 GPa and 900 °C are denoted by the stars. Long dashed line: redox ratios after Kress and Carmichael (1991) calculated at 2 GPa and 900 °C. Short-dashed lines: redox ratio from Wilke *et al.* (2002) at 0.5 GPa. The coloured areas correspond to the predicted $\text{Fe}^{3+}/\text{Fe}^{2+}$ ratio in the $\text{H}_2\text{O} + \text{melt}$ and the $\text{H}_2\text{O-NaCl} + \text{melt}$ system extrapolated from experimental data at 2 GPa and 900 °C to lower temperature conditions. The reported numbers correspond to the amount of Fe_2O_3 , expressed in wt. %.

Supplementary Information References

- Ague, J.J., Tassara, S., Holycross, M.E., Li, J.-L., Cottrell, E., Schwarzenbach, E.M., Fassoulas, C., John, T. (2022) Slab-derived devolatilization fluids oxidized by subducted metasedimentary rocks. *Nature Geoscience* 15, 320–326. <https://doi.org/10.1038/s41561-022-00904-7>
- Ardia, P., Giordano, D., Schmidt, M.W. (2008) A model for the viscosity of rhyolite as a function of H₂O-content and pressure: A calibration based on centrifuge piston cylinder experiments. *Geochimica et Cosmochimica Acta* 72, 6103–6123. <https://doi.org/10.1016/j.gca.2008.08.025>
- Ardia, P., Di Muro, A., Giordano, D., Massare, D., Sanchez-Valle, C., Schmidt, M.W. (2014) Densification mechanisms of haplogranite glasses as a function of water content and pressure based on density and Raman data. *Geochimica et Cosmochimica Acta* 138, 158–180. <https://doi.org/10.1016/j.gca.2014.03.022>
- Blatter, D.L., Carmichael, I.S.E. (1998) Hornblende peridotite xenoliths from central Mexico reveal the highly oxidized nature of subarc upper mantle. *Geology* 26, 1035–1038. [https://doi.org/10.1130/0091-7613\(1998\)026%3C1035:HPXFCM%3E2.3.CO;2](https://doi.org/10.1130/0091-7613(1998)026%3C1035:HPXFCM%3E2.3.CO;2)
- Bose, K., Ganguly, J. (1995) Quartz-coesite transition revisited: reversed experimental determination at 500–1200°C and retrieved thermochemical properties. *American Mineralogist* 80, 231–238. <https://doi.org/10.2138/am-1995-3-404>
- Botcharnikov, R.E., Koepke, J., Holtz, F., McCammon, C., Wilke, M. (2005) The effect of water activity on the oxidation and structural state of Fe in a ferro-basaltic melt. *Geochimica et Cosmochimica Acta* 69, 5071–5085. <https://doi.org/10.1016/j.gca.2005.04.023>
- Bureau, H., Keppler, H. (1999) Complete miscibility between silicate melts and hydrous fluids in the upper mantle: Experimental evidence and geochemical implications. *Earth and Planetary Science Letters* 165, 187–196. [https://doi.org/10.1016/S0012-821X\(98\)00266-0](https://doi.org/10.1016/S0012-821X(98)00266-0)
- Cannaò, E., Malaspina, N. (2018) Geosphere From oceanic to continental subduction : implications for the geochemical and redox evolution of the supra-subduction mantle. *Geosphere* 14, 2311–2336. <https://doi.org/10.1130/GES01597.1>
- Carbonin, S., Martin, S., Tumiatei, S., Rossetti, P. (2015) Magnetite from the Cogne serpentinites (Piemonte ophiolite nappe, Italy). Insights into seafloor fluid–rock interaction. *European Journal of Mineralogy* 27, 31–50. <https://doi.org/10.1127/ejm/2014/0026-2410>
- Connolly, J.A.D. (1995) Phase diagram methods for graphitic rocks and application to the system C–O–H–FeO–TiO₂–SiO₂. *Contributions to Mineralogy and Petrology* 119, 94–116. <https://doi.org/10.1007/BF00310720>
- Debret, B., Bolfan-Casanova, N., Padron-Navarta, J.A., Martin-Hernandez, F., Andreani, M., Garrido, C.J., Sánchez-Vizcaíno V.L., Gómez-Pugnaire M.T., Muñoz, M., Trcera, N. (2015) Redox state of iron during high-pressure serpentinite dehydration. *Contributions to Mineralogy and Petrology* 169, 1–18. <https://doi.org/10.1007/s00410-015-1130-y>
- Evans, K.A. (2006) Redox decoupling and redox budgets: Conceptual tools for the study of earth systems. *Geology* 34, 489–492. <https://doi.org/10.1130/G22390.1>
- Evans, K.A. (2012) The redox budget of subduction zones. *Earth-Science Reviews* 113, 11–32. <https://doi.org/10.1016/j.earscirev.2012.03.003>
- Evans, K.A., Tomkins, A.G. (2011) The relationship between subduction zone redox budget and arc magma fertility. *Earth and Planetary Science Letters* 308, 401–409. <https://doi.org/10.1016/j.epsl.2011.06.009>
- Facq, S., Daniel, I., Montagnac, G., Cardon, H., Sverjensky, D.A. (2014) In situ Raman study and thermodynamic model of aqueous carbonate speciation in equilibrium with aragonite under subduction zone conditions. *Geochimica et Cosmochimica Acta* 132, 375–390. <https://doi.org/10.1016/j.gca.2014.01.030>
- Gaillard, F., Scaillet, B., Pichavant, M. (2002) Kinetics of iron oxidation-reduction in hydrous silicic melts. *American Mineralogist* 87, 829–837. <https://doi.org/10.2138/am-2002-0704>
- Helgeson, H.C., Kirkham, D.H., Flowers, G.C. (1981) Theoretical prediction of the thermodynamic behavior of aqueous electrolytes by high pressures and temperatures; IV, Calculation of activity coefficients, osmotic coefficients, and apparent molal and



- standard and relative partial molal properties to 600. *American Journal of Science*, 1249–1516. <https://doi.org/10.2475/ajs.281.10.1249>
- Hermann, J., Spandler, C., Hack, A., Korsakov, A.V. (2006) Aqueous fluids and hydrous melts in high-pressure and ultra-high pressure rocks: Implications for element transfer in subduction zones. *Lithos* 92, 399–417. <https://doi.org/10.1016/j.lithos.2006.03.055>
- Hermann, J., Spandler, C.J. (2008) Sediment melts at sub-arc depths: An experimental study. *Journal of Petrology* 49, 717–740. <https://doi.org/10.1093/petrology/egm073>
- Holland, T.J.B., Powell, R. (1998) An internally consistent thermodynamic data set for phases of petrological interest. *Journal of Metamorphic Geology* 16, 309–343. <https://doi.org/10.1111/j.1525-1314.1998.00140.x>
- Huang, F., Sverjensky, D.A. (2019) Extended Deep Earth Water Model for predicting major element mantle metasomatism. *Geochimica et Cosmochimica Acta* 254, 192–230. <https://doi.org/10.1016/j.gca.2019.03.027>
- Ionov, D.A., Bénard, A., Plechov, P.Y. (2011) Melt evolution in subarc mantle: Evidence from heating experiments on spinel-hosted melt inclusions in peridotite xenoliths from the andesitic Avacha volcano (Kamchatka, Russia). *Contributions to Mineralogy and Petrology* 162, 1159–1174. <https://doi.org/10.1007/s00410-011-0645-0>
- Kent, A.J.R., Peate, D.W., Newman, S., Stolper, E.M., Pearce, J.A. (2002) Chlorine in submarine glasses from the Lau Basin: Seawater contamination and constraints on the composition of slab-derived fluids. *Earth and Planetary Science Letters* 202, 361–377. [https://doi.org/10.1016/S0012-821X\(02\)00786-0](https://doi.org/10.1016/S0012-821X(02)00786-0)
- Klemme, S., O'Neill, H.S.C. (1997) The reaction $\text{MgCr}_2\text{O}_4 + \text{SiO}_2 = \text{Cr}_2\text{O}_3 + \text{MgSiO}_3$ and the free energy of formation of magnesiochromite (MgCr_2O_4). *Contributions to Mineralogy and Petrology* 130, 59–65. <https://doi.org/10.1007/s004100050349>
- Kress, V.C., Carmichael, I.S.E. (1991) The compressibility of silicate liquids containing Fe_2O_3 and the effect of composition, temperature, oxygen fugacity and pressure on their redox states. *Contributions to Mineralogy and Petrology* 108, 82–92. <https://doi.org/10.1007/BF00307328>
- Louvel, M., Sanchez-Valle, C., Malfait, W., Pokrovski, G., Borca, C., Grolimund, D. (2020) Bromine speciation and partitioning in slab-derived aqueous fluids and silicate melts and implications for halogens transfer in subduction zones. *Solid Earth* 11(4), 1145–1161. <https://doi.org/10.5194/se-11-1145-2020>
- Manning, C.E., Antignano, A., Lin, H.A. (2010) Premelting polymerization of crustal and mantle fluids, as indicated by the solubility of albite+paragonite+quartz in H_2O at 1 GPa and 350–620°C. *Earth and Planetary Science Letters* 292, 325–336. <https://doi.org/10.1016/j.epsl.2010.01.044>
- Marschall, H.R., Schumacher, J.C. (2012) Arc magmas sourced from mélange diapirs in subduction zones. *Nature Geoscience* 5, 862–867. <https://doi.org/10.1038/ngeo1634>
- Mysen, B.O. (2006) The structural behavior of ferric and ferrous iron in aluminosilicate glass near meta-aluminosilicate joins. *Geochimica et Cosmochimica Acta* 70, 2337–2353. <https://doi.org/10.1016/j.gca.2006.01.026>
- Newton, R.C., Manning, C.E. (2008) Thermodynamics of SiO_2 - H_2O fluid near the upper critical end point from quartz solubility measurements at 10 kbar. *Earth and Planetary Science Letters* 274, 241–249. <https://doi.org/10.1016/j.epsl.2008.07.028>
- Nielsen, S.G., Marschall, H.R. (2017) Geochemical evidence for mélange melting in global arcs. *Science Advances* 3, 1–7. <https://doi.org/10.1126/sciadv.1602402>
- Prescher, C., McCammon, C., Dubrovinsky, L. (2012) MossA: A program for analyzing energy-domain Mössbauer spectra from conventional and synchrotron sources. *Journal of Applied Crystallography* 45, 329–331. <https://doi.org/10.1107/S0021889812004979>
- Shock, E.L., Helgeson, H.C. (1988) Calculation of the thermodynamic and transport properties of aqueous species at high pressures and temperatures: Correlation algorithms for ionic species and equation of state predictions to 5 kb and 1000°C. *Geochimica et Cosmochimica Acta* 52, 2009–2036. [https://doi.org/10.1016/0016-7037\(88\)90181-0](https://doi.org/10.1016/0016-7037(88)90181-0)
- Shock, E.L., Helgeson, H.C. (1990) Calculation of the thermodynamic and transport properties of aqueous species at high pressures and temperatures: Standard partial molal properties of organic species. *Geochimica et Cosmochimica Acta* 54, 915–945. [https://doi.org/10.1016/0016-7037\(90\)90429-O](https://doi.org/10.1016/0016-7037(90)90429-O)
- Shock, E.L., Helgeson, H.C., Sverjensky, D.A. (1989) Calculation of the thermodynamic and transport properties of aqueous species



- at high pressures and temperatures: Standard partial molal properties of inorganic neutral species. *Geochimica et Cosmochimica Acta* 53, 2157–2183. [https://doi.org/10.1016/0016-7037\(89\)90341-4](https://doi.org/10.1016/0016-7037(89)90341-4)
- Shock, E.L., Sassani, D.C., Willis, M., Sverjensky, D.A. (1997) Inorganic species in geologic fluids: Correlations among standard molal thermodynamic properties of aqueous ions and hydroxide complexes. *Geochimica et Cosmochimica Acta* 61, 907–950. [https://doi.org/10.1016/S0016-7037\(96\)00339-0](https://doi.org/10.1016/S0016-7037(96)00339-0)
- Sverjensky, D.A. (2019) Thermodynamic modelling of fluids from surficial to mantle conditions. *Journal of the Geological Society* 176, 348–374. <https://doi.org/10.1144/jgs2018-105>
- Sverjensky, D.A., Harrison, B., Azzolini, D. (2014) Water in the deep Earth: The dielectric constant and the solubilities of quartz and corundum to 60kb and 1200°C. *Geochimica et Cosmochimica Acta* 129, 125–145. <https://doi.org/10.1016/j.gca.2013.12.019>
- Syracuse, E.M., van Keken, P.E., Abers, G.A. (2010) The global range of subduction zone thermal models. *Physics of the Earth and Planetary Interiors* 183, 73–90. <https://doi.org/10.1016/j.pepi.2010.02.004>
- Tanger, J.C., Helgeson, H.C. (1988) Calculation of the thermodynamic and transport properties of aqueous species at high pressures and temperatures; revised equations of state for the standard partial molal properties of ions and electrolytes. *American Journal of Science*, 19–98. <https://doi.org/10.2475/ajs.288.1.19>
- Tumiati, S., Godard, G., Martin, S., Malaspina, N., Poli, S. (2015) Ultra-oxidized rocks in subduction mélanges? Decoupling between oxygen fugacity and oxygen availability in a Mn-rich metasomatic environment. *Lithos* 226, 116–130. <https://doi.org/10.1016/j.lithos.2014.12.008>
- Van Keken, P.E., Hacker, B.R., Syracuse, E.M., Abers, G.A. (2011) Subduction factory: 4. Depth-dependent flux of H₂O from subducting slabs worldwide. *Journal of Geophysical Research: Solid Earth* 116. <https://doi.org/10.1029/2010JB007922>
- Wilke, M., Behrens, H., Burkhard, D.J.M., Rossano, S. (2002) The oxidation state of iron in silicic melt at 500 MPa water pressure. *Chemical Geology* 189, 55–67. [https://doi.org/10.1016/S0009-2541\(02\)00042-6](https://doi.org/10.1016/S0009-2541(02)00042-6)
- Wohlert, A., Manning, C.E., Thompson, A.B. (2011). Experimental investigation of the solubility of albite and jadeite in H₂O, with paragonite + quartz at 500 and 600 C, and 1–2.25 GPa. *Geochimica et Cosmochimica Acta* 75, 2924–2939. <https://doi.org/10.1016/j.gca.2011.02.028>
- Wolery, T.J. (1992) EQ3NR, A Computer Program for Geochemical Aqueous Speciation-Solubility Calculations: Theoretical Manual, User's Guide, and Related Documentation (Version 7.0). 262. <https://doi.org/10.2172/138643>

